# Direct observation of current-induced nonlinear spin torque in Pt-Py bilayers

Toshiyuki Kodama [1,*], Nobuaki Kikuchi [2], Takahiro Chiba [3], Satoshi Okamoto [2,4]

Seigo Ohno [5], and Satoshi Tomita [1,5,†]

[1]*Institute for Excellence in Higher Education, Tohoku University, Sendai 980-8576, Japan*

[2]*Institute of Multidisciplinary Research for Advanced Materials, Tohoku University, Sendai 980-8577, Japan*

[3]*Frontier Research Institute for Interdisciplinary Sciences, Tohoku University, Sendai 980-8578, Japan*

[4]*Center for Science and Innovation in Spintronics, Tohoku University, Sendai 980-8577, Japan*

[5]*Department of Physics, Graduate School of Science, Tohoku University, Sendai 980-8578, Japan*

We experimentally observe nonlinear spin torque in metallic bilayers of platinum and permalloy by means of spin-torque ferromagnetic resonance (ST-FMR) under massive dc current injection. The observed nonlinear spin torque exerted on permalloy magnetization is attributed primarily to nonlinear spin polarization. An additional origin of the nonlinear spin torque is magnon generation (annihilation) followed by shrinkage (expansion) of effective magnetization, which is revealed by ST-FMR and unidirectional spin Hall magnetoresistance measurements. The present paper paves a way to spin Hall effect based nonlinear spintronic devices as well as time-varying nonlinear magnetic metamaterials with tailormade permeability.

## I. INTRODUCTION

Nonlinear phenomena are common and intriguing topics in condensed matter physics [1]. Among the fascinating achievements in spintronics and magnonics are nonlinear spin-torque oscillators [2,3], nonlinear spin-wave interference toward memory or neural network systems [4,5], and nonlinear magnon polaritons for quantum information technologies [6]. Recently, several theoretical studies predicted nonlinear spin polarization in noncentrosymmetric systems [7], $\mathcal{PT}$-symmetric collinear magnets [8], and time-reversal centrosymmetric materials [9,10]. The nonlinear spin polarization is of great interest because it probes novel band geometric quantities and offers new tools to characterize and control material properties. However, lacking are experimental studies of the nonlinear spin polarization. Therefore, in this paper, we investigate experimentally the nonlinear spin polarization using spin-torque ferromagnetic resonance (ST-FMR).

When electric current flows in a bilayer system consisting of heavy metal, for example, platinum (Pt), and ferromagnetic metal, for example, permalloy (Py), the spin Hall effect due to strong spin-orbit interaction in the Pt layer gives rise to spin polarization. The spin polarization causes spin current injected to the Py layer, bringing about spin torque exerted on precessing Py magnetization on resonance under magnetic fields; this is referred to as ST-FMR [11]. In this paper, we carry out ST-FMR measurements under large dc current injection up to 20 mA ($\approx 6.5 \times 10^{11}$ A/m$^2$) to directly observe current-induced nonlinear spin torque in Pt-Py bilayers. An undoped silicon (Si) substrate with excellent thermal conductivity enables us to inject such a large current without sample degradation due to the Joule heating. The ST-FMR signals demonstrate that the massive dc current affects the resonance field and Gilbert damping parameter nonlinearly. The nonlinear changes are traced back to the nonlinear spin torque caused by the nonlinear spin polarization. Furthermore, ST-FMR study reveals that the nonlinear spin torque is attributed also to magnon generation (annihilation) followed by effective magnetization shrinkage (expansion), which is confirmed by the observation of unidirectional spin Hall magnetoresistance (USMR) [12].

Eventually we evaluate the origins of the nonlinear spin torque, i.e., the nonlinear spin polarization and magnon generation/annihilation, by introducing indices of nonlinearity, $\eta$ and $\xi$, obtained from ST-FMR and USMR measurements. The experimentally evaluated $\eta$ is larger than $\xi$, indicating that the nonlinear spin polarization is dominant rather than the magnon generation/annihilation in the nonlinear spin torque. The $\eta$ and $\xi$ correspond respectively to the second- and third-order nonlinear susceptibilities, $\chi^{(2)}$ and $\chi^{(3)}$, in nonlinear photonics [1]. In analogy between photonics and electronics, $\eta$ and $\xi$ can be used to evaluate spintronic nonlinearity, elucidate the origins of nonlinear phenomena, and realize nonlinear spintronic effects, for example, second harmonic generation and rectification. Furthermore, the nonlinear spin torque leads to time-varying nonlinear magnetic metamaterials for sixth-generation mobile communication light sources of millimeter waves and terahertz light [13].

## II. EXPERIMENTAL SETUP

We study metallic bilayers composed of a 5-nm-thick Pt top layer and 2-nm-thick Py bottom layer. The Pt-Py bilayer is deposited after a 3-nm-thick tantalum buffer layer on an undoped Si substrate having electrical resistivity at least 1 k$\Omega$ cm (Crystal Base, Inc.) [13]. An inset of
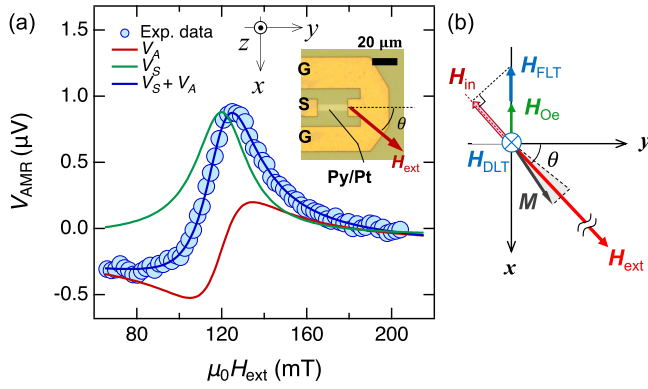
*tkodama@tohoku.ac.jp

†tomita@tohoku.ac.jp

FIG. 1. (a) Measured ST-FMR signal (blue circles), as a function of external dc magnetic field, $\mu_0 H_{ext}$, with $I_{ac}$ at 9 GHz. Green and red solid lines represent fitting curves with symmetric ($V_S$) and antisymmetric coefficients ($V_A$), respectively. The blue solid line corresponds to the sum of $V_S$ and $V_A$. Inset: Optical microscopic image of the Py-Pt bilayer strip with Au electrodes. (b) Schematic of Py magnetization ($M$), $H_{ext}$, and Oersted field ($H_{Oe}$). Effective fields $H_{FLT}$ and $H_{DLT}$ correspond to fieldlike torque and dampinglike torque, respectively. In-plane effective field $H_{in}$ is a component of $H_{FLT}$ and $H_{Oe}$ parallel to $H_{ext}$.

## III. RESULTS

### A. Spin-torque ferromagnetic resonance measurement

Figure 1(a) shows a typical ST-FMR signal probed by $V_{AMR}$ with $I_{ac}$ at 9 GHz. The blue circles correspond to measured $V_{AMR}$. The $V_{AMR}$ in a thin film is expressed as $V_{AMR} = V_S + V_A$, where $V_S$ and $V_A$ are symmetric and antisymmetric components, respectively [11]. Both $V_S$ and $V_A$ are described using $\mu_0 H_{ext}$, the resonance field ($\mu_0 H_{FMR}$), and the half width at half maximum ($\mu_0 \Delta_{FMR}$) of the FMR signal. The fitting in Fig. 1(a) gives $\mu_0 H_{FMR} = 119.8$ mT and $\mu_0 \Delta_{FMR} = 14.8$ mT. The sum of $V_S$ (green line) and $V_A$ (red line) after the fitting is represented by the blue line, which reproduces well the measured $V_{AMR}$.
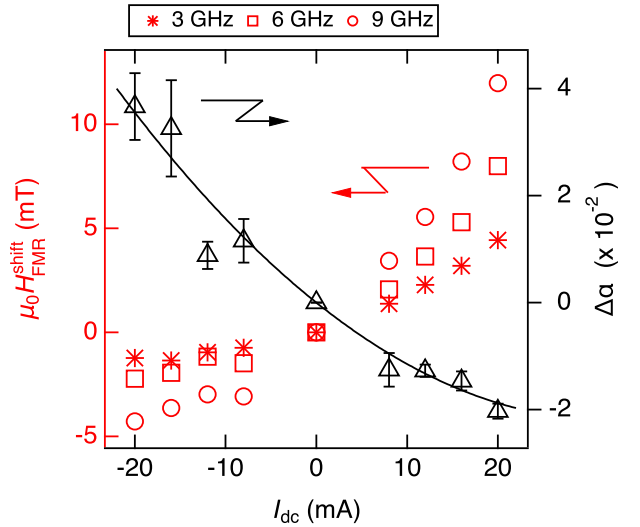
Fig. 1(a) shows an optical microscopic image of the specimen consisting of a lithographically prepared Pt-Py strip attached to gold electrodes. The width of the strip is 5 μm and the length is 24 μm. In ST-FMR measurements, an in-plane external dc magnetic field $H_{ext}$ is applied with a relative angle $\theta = 45°$ to the $y$ axis as shown in Figs. 1(a) and 1(b). An ac current $I_{ac}$ with microwave frequencies is applied between the signal (S) and ground (G) lines by a signal generator. The $I_{ac}$ in the Pt layer generates an oscillating Oersted magnetic field, which primarily drives ST-FMR of the Py magnetization $M$. Additionally, the spin Hall effect in the Pt layer gives rise to ac spin current, which is injected into the Py layer. The spin angular momentum is transferred to the in-plane Py magnetization, exerting a fieldlike torque (FLT) that secondary drives ST-FMR and a dampinglike torque (DLT) that enhances or reduces magnetic relaxation [14–16]. Mixing of $I_{ac}$ and oscillating anisotropic magnetoresistance (AMR) in Py gives rise to a time-independent longitudinal dc voltage $V_{AMR}$. We measure $V_{AMR}$ as a function of $\mu_0 H_{ext}$ using a bias tee to obtain ST-FMR signals. All measurements are carried out at room temperature.



FIG. 2. $I_{dc}$ vs resonance field shift $\mu_0 H_{FMR}^{shift}$ (left axis) with $I_{ac}$ at 3 GHz (red asterisks), 6 GHz (red squares), and 9 GHz (red circles). Gilbert damping parameter variation $\Delta\alpha$ (right axis, black triangles) reproduced from our previous report [13] is also plotted as a function of $I_{dc}$. The solid line corresponds to the fitting curve.

Together with $I_{ac}$, a dc current $I_{dc}$ is applied to the bilayer to modify the FMR condition [17,18]. The $I_{dc} > 0$ ($I_{dc} < 0$) corresponds to the current in the $+y$ ($-y$) direction. The $I_{dc}$ causes a time-independent dc Oersted field $\boldsymbol{H}_{Oe}$ along the $\pm x$ axis as shown in Fig. 1(b). Additionally, $I_{dc}$ generates a time-independent FLT and DLT on $\boldsymbol{M}$. As in Fig. 1(b), FLT and DLT are regarded as effective fields $\boldsymbol{H}_{FLT} \propto \delta s$ and $\boldsymbol{H}_{DLT} \propto \boldsymbol{m} \times \delta s$, respectively. The $\delta s$ is spin polarization and $\boldsymbol{m}$ is a unit vector of magnetization [19,20]. The $\boldsymbol{H}_{FLT}$ and $\boldsymbol{H}_{DLT}$ affect the FMR condition, resulting in a shift of $\mu_0 H_{FMR}$ and a change in $\mu_0 \Delta_{FMR}$.

To study the shift of $\mu_0 H_{FMR}$ and change in $\mu_0 \Delta_{FMR}$ by $\boldsymbol{H}_{FLT}$ and $\boldsymbol{H}_{DLT}$, the ST-FMR signals with $I_{dc}$ between $-20$ and $+20$ mA are measured at various $I_{ac}$ frequency ($f_{ac}$) from 3 to 9 GHz. Thanks to the undoped Si substrate with a better thermal conductivity of 150 W/mK [21] compared to quartz (1.4 W/mK) [22] and magnesium oxide (56 W/mK) [23] substrates, a large $I_{dc}$ up to $\pm 20$ mA can be applied (see Supplemental Material SM1 [24]). After the fitting of the ST-FMR signals, we evaluate $\mu_0 H_{FMR}$ and $\mu_0 \Delta_{FMR}$ at a specific $I_{dc}$ value. The resonance field shift $\mu_0 H_{FMR}^{shift}$ by $I_{dc}$ injection is derived from $\mu_0 H_{FMR}^{shift}(I_{dc}) = \mu_0 H_{FMR}(I_{dc}) - \mu_0 H_{FMR}(0)$, where $\mu_0 H_{FMR}(I_{dc})$ corresponds to $\mu_0 H_{FMR}$ at nonzero $I_{dc}$ and $\mu_0 H_{FMR}(0)$ corresponds to $\mu_0 H_{FMR}$ at zero $I_{dc}$. Moreover, $f_{ac}$ dependence of $\mu_0 \Delta_{FMR}$ gives Gilbert damping parameter $\alpha$ at a specific $I_{dc}$ value.

Figure 2 shows $I_{dc}$ versus $\mu_0 H_{FMR}^{shift}$ at $f_{ac} = 3$ GHz (red asterisks), 6 GHz (red squares), and 9 GHz (red circles) as indicated from the left vertical axis. In addition, the variation in $\alpha$ by $I_{dc}$ injection, $\Delta\alpha(I_{dc}) = \alpha(I_{dc}) - \alpha(0)$, reproduced from our previous report [13], is plotted as black triangles indicated from the right vertical axis. The $\mu_0 H_{FMR}^{shift}$ and $\Delta\alpha$ are odd functions of $I_{dc}$, because $\delta s$ is an odd function of the dc current. Figure 2 highlights two striking features: (i) $\mu_0 H_{FMR}^{shift}$ and $\Delta\alpha$ are dependent nonlinearly on $I_{dc}$, and (ii) a higher $f_{ac}$
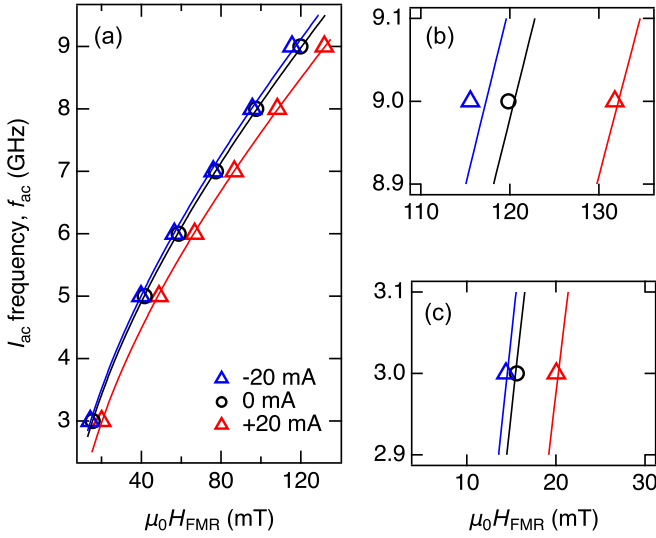
FIG. 3. (a) $I_{ac}$ frequency ($f_{ac}$) vs $\mu_0 H_{FMR}$ at $I_{dc} = -20$ mA (blue triangles), 0 mA (black circles), and $+20$ mA (red triangles). Solid lines: Fitting curves using the Kittel equation [Eq. (1)]. (b), (c) Enlarged figure of (a).
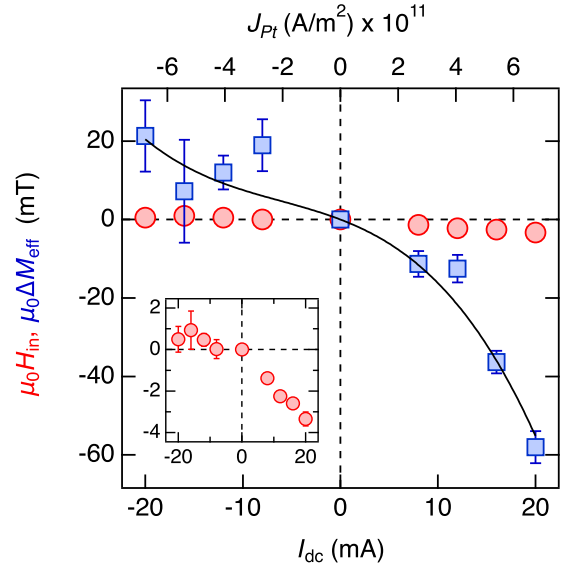


FIG. 4. In-plane effective field $\mu_0 H_{in}$ (red circles) and effective magnetization variation $\mu_0 \Delta M_{eff}$ (blue squares) are plotted as a function of $I_{dc}$. Inset: Enlarged view for $\mu_0 H_{in}$. The current density in the Pt layer converted from $I_{dc}$ is indicated from the upper horizontal axis. The solid line corresponds to a fitting curve. Error bars are the standard deviation of the fitting.

results in a larger $|\mu_0 H_{FMR}^{shift}|$ at the same $I_{dc}$. Note that these features are observed in another specimen with a longer Pt-Py strip of 45-μm length (see Supplemental Material SM2 [24]).

### B. Evaluation of variation in effective magnetization

The $\mu_0 H_{FMR}$ with various $I_{dc}$ of $-20$, 0, and 20 mA are plotted as a function of $f_{ac}$ from 3 to 9 GHz in Fig. 3. Blue triangles, black circles, and red triangles correspond respectively to $\mu_0 H_{FMR}$ by $I_{dc} = -20$, 0, and 20 mA. Figures 3(b) and 3(c) show enlarged plots of Fig. 3(a), in which the horizontal axis variations are identical at 25 mT for direct comparison. At $f_{ac} = 3$ GHz as in Fig. 3(c), the resonance field shifts upward by 5.7 mT when $I_{dc}$ increases from $-20$ to 20 mA. At a higher $f_{ac}$ of 9 GHz as in Fig. 3(b), the shift amount is larger at 16.2 mT.

As shown in Fig. 1(b), a component of $H_{FLT}$ and $H_{Oe}$ parallel to the $H_{ext}$ corresponds to the in-plane effective field $H_{in}$. The $H_{in}$ expressed as $\mu_0 H_{in} = (\mu_0 H_{FLT} + \mu_0 H_{Oe}) \times \sin\theta$, where $\theta = \pi/4$ in the present ST-FMR study, is small, but affects the FMR condition (see Supplemental Material SM3 [24]). The Kittel equation for FMR is described as

$$2\pi f_{ac} = \gamma \sqrt{\mu_0 H_{FMR}(I_{dc} = 0) + \mu_0 H_{in}}$$
$$\times \sqrt{\mu_0 H_{FMR}(I_{dc} = 0) + \mu_0 H_{in} + \mu_0 M_{eff}}, \quad (1)$$

where $\gamma$ is the gyromagnetic ratio, $\mu_0 H_{FMR}(I_{dc} = 0)$ is the resonance field without $I_{dc}$ injection, and $\mu_0 M_{eff}$ is the effective magnetization. When $I_{dc} = 0$ mA, the black circles in Fig. 3 are fitted by Eq. (1) with $\mu_0 H_{in} = 0$. The fitting gives $\mu_0 M_{eff}(I_{dc} = 0) = \mu_0 M_s = 658$ mT, where $\mu_0 M_s$ is the saturation magnetization. The $\mu_0 M_s$ of 658 mT is smaller than a typical value of Py saturation magnetization, probably due to magnetic dead layers at the Pt-Py interface [13,25].

Equation (1) is fitted to $\mu_0 H_{FMR}$ at $I_{dc} = \pm 8$, $\pm 12$, $\pm 16$, and $\pm 20$ mA to evaluate $\mu_0 M_{eff}$ and $\mu_0 H_{in}$. The fitting curves with $I_{dc} = -20$ and $+20$ mA are drawn by blue and red

solid lines in Fig. 3, respectively. In Fig. 4, evaluated $\mu_0 H_{in}$ (red circles) and $\mu_0 \Delta M_{eff} = \mu_0 M_{eff} - \mu_0 M_s$ (blue square) are plotted as a function of $I_{dc}$. The upper horizontal axis indicates the $J_{Pt}$, electrical current density in the Pt layer (see Supplemental Material SM4 [24]). The inset shows an enlarged view of $\mu_0 H_{in}$ versus $I_{dc}$. The $\mu_0 H_{in}$ is very small, slightly decreases with increasing $I_{dc}$, and reaches $-3.3$ mT when $I_{dc}$ is 20 mA.

Contrastingly, $\mu_0 \Delta M_{eff}$ is affected significantly by $I_{dc}$. The maximum value of $\mu_0 \Delta M_{eff}$ at $I_{dc} = 20$ mA is $-60$ mT, which includes $\mu_0 H_{DLT}$ as shown in Fig. 1(b). However, $\mu_0 \Delta M_{eff} = -60$ mT is nonetheless larger than the $\mu_0 H_{DLT}$ evaluated from previous reports, for example, $-2.4$ mT at approximately $I_{dc} = 20$ mA ($\approx 6.5 \times 10^{11} \text{A/m}^2$) in Ref. [20]. Note here that $\mu_0 H_{FMR}$ with nonzero $I_{dc}$ in Fig. 3 cannot be reproduced using Eq. (1) without $\mu_0 \Delta M_{eff}$. This is clearly indicated in Eq. (1), i.e., $\mu_0 H_{in}$ shifts the curves whereas $\mu_0 \Delta M_{eff}$ changes the gradient of the curves. The large $\mu_0 \Delta M_{eff}$ is indispensable in explaining a larger resonance field shift at a higher $f_{ac}$. The negative $\mu_0 \Delta M_{eff}$ corresponds to shrinkage of $\mu_0 M_{eff}$, whereas the positive $\mu_0 \Delta M_{eff}$ corresponds to expansion. Therefore, we consider shrinkage/expansion of effective magnetization by nonlinear magnon generation/annihilation.

### C. Unidirectional spin Hall magnetoresistance measurement

The nonlinear magnon generation/annihilation due to massive spin current injection likely brings about USMR [26,27]. We thus conduct USMR measurements with the large $I_{dc}$ injection using the same specimen. Figures 5(a) and 5(b) show schematics of the sample cross section in the $x$-$z$ plane viewed in the $+y$ direction. The $\theta$ is $+90°$ or $-90°$ in the USMR measurements, i.e., the $\mu_0 H_{ext} = +100$ mT is applied to the sample in the $+x$ direction [Fig. 5(a)], while $\mu_0 H_{ext} = -100$ mT in the $-x$ direction [Fig. 5(b)]. The dc current $I_{dc}$
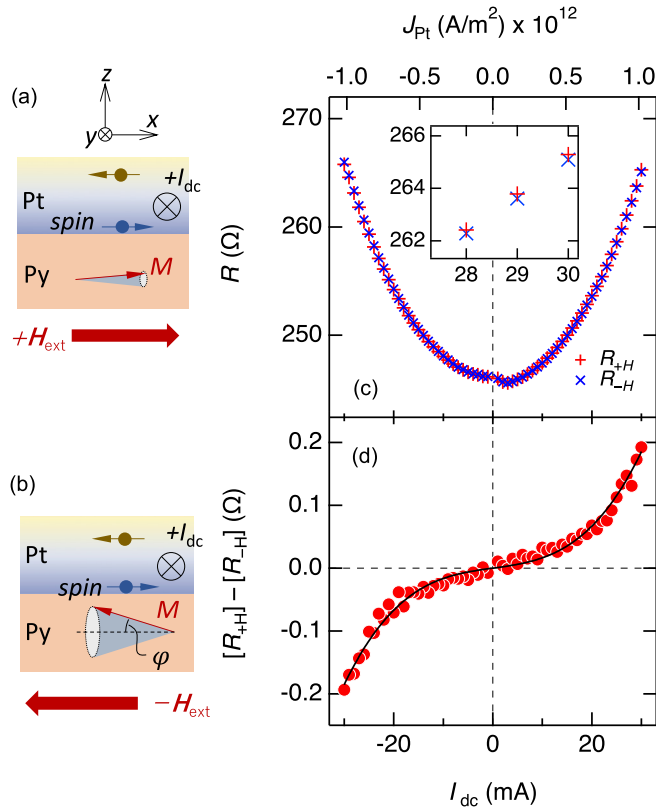
FIG. 5. Schematics of the specimen cross section for (a) $R_{+H}$ under $\mu_0 H_{ext} = +100$ mT and (b) $R_{-H}$ under $\mu_0 H_{ext} = -100$ mT. (c) $I_{dc}$ vs electric resistance $R_{+H}$ and $R_{-H}$. The current density in the Pt layer converted from $I_{dc}$ is indicated from the upper horizontal axis. Inset: Enlarged view around 30 mA. (d) Difference between the electric resistance under $\mu_0 H_{ext} = +100$ and $-100$ mT; $[R_{+H}] - [R_{-H}]$ is plotted as a function of $I_{dc}$. The solid line corresponds to the fitting curve.

between $-30$ and $+30$ mA is chopped to be 0.2-ms-width pulses. The longitudinal dc voltage $V_{dc}$ is measured 100 times to obtain an averaged value of $V_{dc}$.

The measured $V_{dc}$-$I_{dc}$ curve is converted to the dc electric resistance $R$-$I_{dc}$ curve as shown in Fig. 5(c). Red crosses (+) correspond to $R$ under $\mu_0 H_{ext} = +100$ mT, referred to as $R_{+H}$, while blue crosses (×) correspond to $R$ under $\mu_0 H_{ext} = -100$ mT, referred to as $R_{-H}$. Because the current is applied beyond the ohmic region, Fig. 5(c) shows a parabolic increase in $R_{+H}$ and $R_{-H}$ due to the Joule heating [28]. Note here that a very similar increase in $V_{dc}$ is confirmed in a measurement using unchopped continuous $I_{dc}$ as same as in the ST-FMR study (see Supplemental Material SM1 [24]). Figure 5(c) shows that $R_{\pm H}$ increases from 245 Ω at $|I_{dc}| \approx 0$ mA to 255 Ω at $|I_{dc}| \approx 20$ mA. Given that a temperature coefficient of Pt resistance is 0.002 K$^{-1}$, the increase in $R_{\pm H}$ from 245 to 255 Ω corresponds to the sample temperature elevation of approximately 20 K [29]. This evaluation clearly indicates that the Joule heating component is small and not dominant in the present ST-FMR experiments with $|I_{dc}|$ up to 20 mA.

As highlighted in the inset of Fig. 5(c), an enlarged view at approximately $I_{dc} = 30$ mA, $R_{+H}$ (red crosses) is slightly larger than $R_{-H}$ (blue crosses). The difference between $R_{+H}$ and $R_{-H}$ is plotted as a function of $I_{dc}$ in Fig. 5(d). Note

TABLE I. Nonlinearity indices $\eta$ and $\xi$ evaluated from ST-FMR and USMR measurements.

| | $\eta$ ( mA)$^{-1}$ | $\xi$ ( mA)$^{-2}$ |
|---|---|---|
| USMR | | $5.25 \times 10^{-3}$ |
| ST-FMR magnetization | $4.56 \times 10^{-2}$ | $2.47 \times 10^{-3}$ |
| ST-FMR damping | $1.54 \times 10^{-2}$ | |

that the small Joule heating contribution, which is independent of the Py magnetization reversal, is already removed in the $[R_{+H}] - [R_{-H}]$ plot. As $I_{dc}$ increases from 0 to 30 mA, $[R_{+H}] - [R_{-H}]$ increases slowly and then rapidly above 20 mA. More strikingly, $[R_{+H}] - [R_{-H}]$ is odd under the $I_{dc}$ direction reversal; this is the hallmark of USMR.

The USMR is caused by the electron scattering by magnons. When the spins are injected into the Py layer, parallel spin injection to the Py magnetization annihilates the magnons as in Fig. 5(a) whereas antiparallel spin injection generates the magnons as in Fig. 5(b). The magnon generation/annihilation influences the electron-magnon scattering, resulting in a resistance change of the Py layer as USMR. The excited magnon number is increased nonlinearly when the inherent damping of Py is compensated by the antidamping DLT [27]. This is consistent with nonlinear decrease in $\Delta\alpha$ observed in Fig. 2. The magnon excitation depending on the current is expressed as $a_{USMR} I_{dc} + c_{USMR} (I_{dc})^3$, where $a_{USMR}$ and $c_{USMR}$ are linear and third-order nonlinear coefficients, respectively [27,30]. The fitting gives parameters of $(a_{USMR}, c_{USMR}) = (1.08 \times 10^{-3}, 5.67 \times 10^{-6})$, resulting in the ratio $\xi_{USMR} = c_{USMR}/a_{USMR} \approx 5.25 \times 10^{-3}$ (mA)$^{-2}$ as summarized in Table I. The fitting curve represented by a black solid line in Fig. 5(d) reproduces well the experimental results. This indicates that the USMR in Fig. 5(d) is traced back to the magnon generation/annihilation.

### D. Magnetization measurement

Magnetization of the Pt-Py bilayer is measured using a vibrating sample magnetometer (VSM). Figure 6(a) shows magnetization curves at 296 K (room temperature, black) and 346 K (red). The magnetization is normalized by the saturation magnetization $\mu_0 M_S$ at 296 K. By elevating the temperature from 296 to 346 K, $\mu_0 M_S$ decreases slightly. In Fig. 6(b), normalized $\mu_0 M_S$ is plotted as a function of temperature (red circles). $\mu_0 M_S$ decreases monotonically as temperature increases. The solid black line is a linear function obtained by the fitting of red circles. The gradient of the linear function is $-1.5 \times 10^{-3}$ K$^{-1}$. When the sample temperature is 316 K, corresponding to 20-K elevation from room temperature, the normalized $\mu_0 M_S$ is 0.97.

### IV. DISCUSSION

The 20-K temperature elevation due to the Joule heating confirmed in the USMR study causes a saturation magnetization decrease by 3% evaluated by magnetization measurements. This value is smaller than the decrease in $|\mu_0 \Delta M_{eff}|$ of 60 mT evaluated in Fig. 4 corresponding to 9% of $\mu_0 M_S = 658$ mT. Moreover, $|\mu_0 \Delta M_{eff}|$ variation is
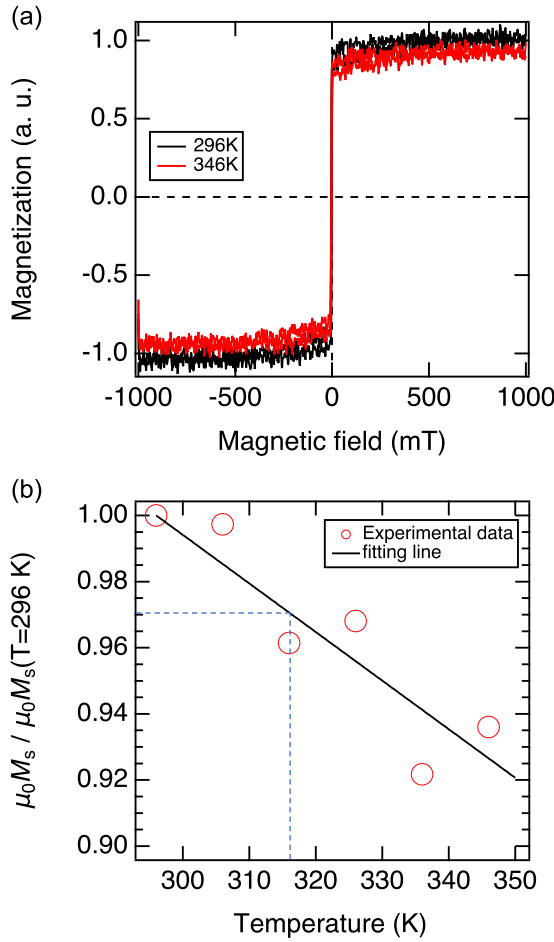
(a)



(b)



FIG. 6. (a) Magnetization curves of the Pt-Py bilayer at 296 (black) and 346 K (red) measured using VSM. (b) Normalized saturation magnetization $\mu_0 M_S$ (red circles) as a function of temperature. The black line shows a fitting result using a linear function. The blue dotted line indicates that at 316 K, which is 20 K higher than room temperature, normalized $\mu_0 M_S$ is 0.97.

asymmetric for the sign of $I_{dc}$. Therefore, the Joule heating is not dominant, indicating that the nonlinear spin polarization [9,10] causes the nonlinear spin torque observed in the present ST-FMR study.

The spin polarization $\delta s_i$ is described by an electronic response to an applied electric field $E_j$ as $\delta s_i = \chi_{ij}^{s(1)} E_j + \chi_{ijk}^{s(2)} E_j E_k$, where $i$, $j$, and $k$ are Cartesian indices and the Einstein summation convention is adopted [9,10]. The $\chi_{ijk}^{s(2)}$ corresponds to the second-order nonlinear response tensor, which is relevant to the Berry connection polarizability determined by the electronic band structures. In Fig. 2, we focus on the nonlinear variation of $\Delta\alpha$ because $\Delta\alpha$ is relevant to the magnitude of spin torque. The nonlinear spin polarization in Pt is partially absorbed by the Py magnetization, resulting in a nonlinear torque ($\propto \delta s \times \mathbf{M}$). In this way, the nonlinear torque caused by the nonlinear spin polarization gives rise to $\Delta\alpha$ depending on $(I_{dc})^2$. Indeed, the variation of $\Delta\alpha$ in Fig. 2 is reproduced well by the fitting curve $a_{damp} I_{dc} + b_{damp} (I_{dc})^2$ as represented by the black solid lines with $(a_{damp}, b_{damp}) = (1.35 \times 10^{-3}, 2.10 \times 10^{-5})$. An index of nonlinearity is

evaluated to be $\eta_{damp} = b_{damp}/a_{damp} \approx 1.54 \times 10^{-2}$ (mA)$^{-1}$ as shown in Table I.

Based on the Holstein-Primakoff picture [31], the magnon number $\langle \hat{a}^\dagger \hat{a} \rangle$ is related to the precession angle $\varphi$ as $\langle \hat{a}^\dagger \hat{a} \rangle = S(1 - \cos\varphi) = 2S\sin(\varphi/2)$, where $\hat{a}^\dagger (\hat{a})$ is the creation (annihilation) operator for magnons and the $S$ is the magnitude squared of the spin angular momentum [32]. Hence, the magnon generation (annihilation), $\delta\langle \hat{a}^\dagger \hat{a} \rangle$, by the spin injection gives rise to the increase (decrease) of the precession angle $\delta\varphi$, which corresponds to shrinkage (expansion) of the effective magnetization in the $x$-axis direction as in Figs. 5(a) and 5(b) [32]. Because the spin torque is expressed as $\propto \delta s \times \mathbf{M}_{eff}$, the nonlinear magnon generation/annihilation confirmed by the USMR study and followed by the magnetization shrinkage/expansion can thus be another origin of the nonlinear spin torque.

Given that the magnetization shrinkage/expansion contains both the second- and third-order nonlinearity [27], $\mu_0 \Delta M_{eff}$ is expressed as $a_{mag} I_{dc} + b_{mag} (I_{dc})^2 + c_{mag} (I_{dc})^3$, where $a_{mag}$, $b_{mag}$, and $c_{mag}$ correspond respectively to the linear coefficient and the second- and third-order nonlinear coefficients. A fitting curve with $(a_{mag}, b_{mag}, c_{mag}) = (9.51 \times 10^{-4}, 4.34 \times 10^{-5}, 2.35 \times 10^{-6})$ represented by a solid black line in Fig. 4 reproduces experimentally obtained values of $\mu_0 \Delta M_{eff}$. The $\xi_{mag} = c_{mag}/a_{mag}$ is $2.47 \times 10^{-3}$ (mA)$^{-2}$, which is similar to $\xi_{USMR} \approx 5.25 \times 10^{-3}$ (mA)$^{-2}$ obtained from USMR measurements. In addition, the $\eta_{mag} = b_{mag}/a_{mag}$ is $\approx 4.56 \times 10^{-2}$ (mA)$^{-1}$, which is similar to $\eta_{damp} \approx 1.54 \times 10^{-2}$ (mA)$^{-1}$ as summarized in Table I.

The present paper reveals that massive $I_{dc}$ causes the nonlinear spin torque. The nonlinear spin torque has two origins at least. The first origin is electronic, i.e., the nonlinear spin polarization in the Pt layer. The nonlinear spin polarization results in nonlinear spin torque directly observed by nonlinear $\Delta\alpha$ variation and represented by $\eta_{damp}$ and $\eta_{mag}$. The second origin is magnonic, i.e., the nonlinear magnon generation/annihilation confirmed by USMR and effective magnetization shrinkage/expansion, and represented by $\xi_{USMR}$ and $\xi_{mag}$. In comparison between $\eta$ and $\xi$, Table I indicates that nonlinear spin polarization is dominant rather than nonlinear magnon generation/annihilation. However, the nonlinear magnon generation/annihilation is caused by the linear spin polarization as well as nonlinear spin polarization [33]. Therefore, the magnonic origin could be comparable to the electronic origin. This is a future issue for theoretical consideration.

The indices $\eta$ and $\xi$ obtained in ST-FMR and USMR measurements are utilized in nonlinear spintronics of magnetic insulators. The nonlinear spin polarization is anticipated to bring about spin-torque oscillation in the Pt-Py bilayer [34,35]. Furthermore, the nonlinear variation of the $\alpha$ and $\mu_0 M_{eff}$ due to the nonlinear spin torque enables us to vary significantly the magnetic permeability of the magnetic bilayer system. Figure 7(a) shows nonlinear variation of $\alpha$ calculated using $\eta = 1.54 \times 10^{-2}$. Nonlinear variation of $\mu_0 M_{eff}$ calculated using $\eta = 4.56 \times 10^{-2}$ and $\xi = 2.47 \times 10^{-3}$ is shown in Fig. 7(b). The relationship between $\mu_0 M_{eff}$ and the FMR resonance frequency $f_{FMR}$ is expressed by the Kittel equation as

$$2\pi f_{FMR} = \omega_{FMR} = \gamma \sqrt{\mu_0 H_{ext}(\mu_0 H_{ext} + \mu_0 M_{eff})}, \quad (2)$$
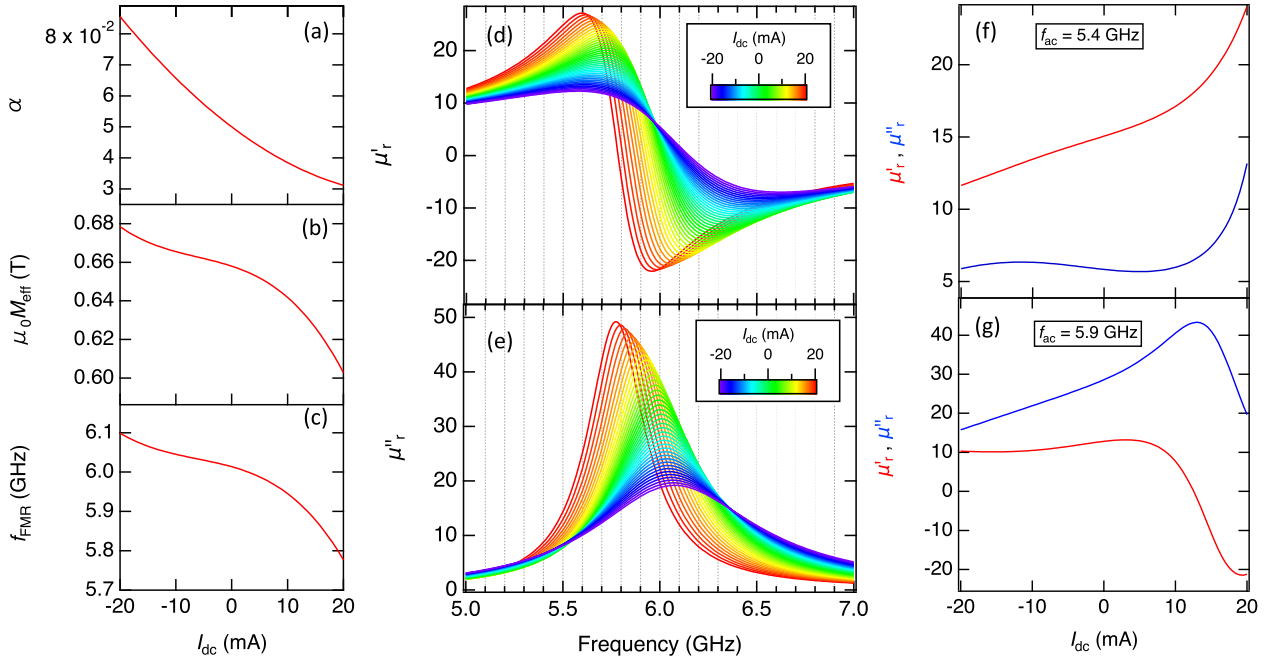
FIG. 7. (a)–(c) Damping parameter $\alpha$ calculated using the nonlinear index of $\eta = 1.54 \times 10^{-2}$, effective magnetization $\mu_0 M_{\text{eff}}$, and resonance frequency $f_{\text{FMR}}$ calculated using the nonlinear index of $\eta = 4.56 \times 10^{-2}$ and $\xi = 2.47 \times 10^{-3}$ plotted as a function of $I_{\text{dc}}$. (d) Real $\mu_r'$ and (e) imaginary $\mu_r''$ parts of the relative magnetic permeability are evaluated using $\alpha$ and $\mu_0 M_{\text{eff}}$, and plotted as a function of frequency. Colors correspond to $I_{\text{dc}}$ values. The $\mu_r'$ and $\mu_r''$ vs $I_{\text{dc}}$ at (f) 5.4 GHz and (g) 5.9 GHz are also shown.

where $\omega_{\text{FMR}}$ is the resonance angular frequency. Nonlinear variation of $\omega_{\text{FMR}}$ is thus obtained as plotted in Fig. 7(c). Using $\alpha$, $\mu_0 M_{\text{eff}}$, and $\omega_{\text{FMR}}$, we evaluate the magnetic permeability variation under a dc external magnetic field $\mu_0 H_{\text{FMR}} = 58.4$ mT. The relative permeability is written by real $\mu_r'$ and imaginary $\mu_r''$ parts [13] as

$$\mu_r(\omega) = \mu_r'(\omega) - j\mu_r''(\omega), \tag{3}$$

where

$$\mu_r'(\omega) = 1 + \gamma \mu_0 M_{\text{eff}} \frac{\omega_{\text{FMR}}(\omega_{\text{FMR}}^2 - \omega^2) + \omega_{\text{FMR}}\omega^2\alpha^2}{\left[\omega_{\text{FMR}}^2 - \omega^2(1+\alpha^2)\right]^2 + 4\omega_{\text{FMR}}^2\omega^2\alpha^2}, \tag{4a}$$

$$\mu_r''(\omega) = \gamma \mu_0 M_{\text{eff}} \frac{\alpha\omega[\omega_{\text{FMR}}^2 - \omega^2(1+\alpha^2)]}{\left[\omega_{\text{FMR}}^2 - \omega^2(1+\alpha^2)\right]^2 + 4\omega_{\text{FMR}}^2\omega^2\alpha^2}. \tag{4b}$$

By substituting $\alpha$, $\mu_0 M_{\text{eff}}$, and $\omega_{\text{FMR}}$ into Eq. (4), $\mu_r(\omega)$ at each $I_{\text{dc}}$ is evaluated.

Figures 7(d) and 7(e) show dispersion curves of $\mu_r'(\omega)$ and $\mu_r''(\omega)$, respectively, at various $I_{\text{dc}}$ from $-20$ (blue) to $+20$ mA (red) at 1-mA intervals. In Fig. 7(f), $\mu_r'$ and $\mu_r''$ obtained at 5.4 GHz are plotted as a function of $I_{\text{dc}}$. When $I_{\text{dc}}$ is varied from $-20$ to 10 mA, only the $\mu_r'$ can be modified. Contrastingly, at 5.9 GHz, only $\mu_r''$ can be modified as in Fig. 7(g). This is advantageous in realizing time-varying permeability

metamaterials for the microwave frequency conversion towards a sixth-generation mobile communication light source.

## V. CONCLUSION

We directly observe the nonlinear spin torque in the Pt-Py bilayer by means of ST-FMR with a large dc current. The nonlinear spin torque observed by nonlinear $\Delta\alpha$ variation is attributed primarily to nonlinear spin polarization represented by $\eta$. Moreover, ST-FMR and USMR measurements demonstrate that nonlinear magnon generation/annihilation followed by shrinkage/expansion of effective magnetization, represented by $\xi$, is another origin of the nonlinear spin torque. Comparison between $\eta$ and $\xi$ indicates that nonlinear spin polarization is dominant rather than nonlinear magnon generation/annihilation. The real and imaginary parts of permeability can be varied independently using nonlinear spin torque. The present paper paves a way to spin Hall effect based nonlinear spintronic devices as well as time-varying nonlinear magnetic metamaterials with tailormade permeability.

[1] R. W. Boyd, *Nonlinear Optics*, 3rd ed. (Academic, New York, 2008).

[2] T. Yamaguchi, N. Akashi, K. Nakajima, S. Tsunegi, H. Kubota, and T. Taniguchi, Synchronization and chaos in a spin-torque

oscillator with a perpendicularly magnetized free layer, Phys. Rev. B **100**, 224422 (2019).

[3] S. Iwakiri, S. Sugimoto, Y. Niimi, K. Kobayashi, Y. Kozuka, Y. K. Takahashi, and S. Kasai, Generation of multipeak spectrum of spin torque oscillator in non-linear regime, Appl. Phys. Lett. **117**, 022406 (2020).

[4] K. Adhikari, S. Sahoo, A. K. Mondal, Y. Otani, and A. Barman, Large nonlinear ferromagnetic resonance shift and strong magnon-magnon coupling in $Ni_{80}Fe_{20}$ nanocross array, Phys. Rev. B **101**, 054406 (2020).

[5] T. Hula, K. Schultheiss, F. J. T. Gonçalves, L. Körber, M. Bejarano, M. Copus, L. Flacke, L. Liensberger, A. Buzdakov, A. Kákay, M. Weiler, R. Camley, J. Fassbender, and H. Schultheiss, Spin-wave frequency combs, Appl. Phys. Lett. **121**, 112404 (2022).

[6] O. Lee, K. Yamamoto, M. Umeda, C. W. Zollitsch, M. Elyasi, T. Kikkawa, E. Saitoh, G. E. W. Bauer, and H. Kurebayashi, Nonlinear magnon polaritons, Phys. Rev. Lett. **130**, 046703 (2023).

[7] K. Hamamoto, M. Ezawa, K. W. Kim, T. Morimoto, and N. Nagaosa, Nonlinear spin current generation in noncentrosymmetric spin-orbit coupled systems, Phys. Rev. B **95**, 224430 (2017).

[8] S. Hayami, M. Yatsushiro, and H. Kusunose, Nonlinear spin Hall effect in PT-symmetric collinear magnets, Phys. Rev. B **106**, 024405 (2022).

[9] C. Xiao, H. Liu, W. Wu, H. Wang, Q. Niu, and S. A. Yang, Intrinsic nonlinear electric spin generation in centrosymmetric magnets, Phys. Rev. Lett. **129**, 086602 (2022).

[10] C. Xiao, H. Liu, W. Wu, H. Wang, Y.-X. Huang, X. Feng, H. Liu, G.-Y. Guo, Q. Niu, and S. A. Yang, Time-reversal-even nonlinear current induced spin polarization, Phys. Rev. Lett. **130**, 166302 (2023).

[11] L. Liu, T. Moriyama, D. C. Ralph, and R. A. Buhrman, Spin-torque ferromagnetic resonance induced by the spin Hall effect, Phys. Rev. Lett. **106**, 036601 (2011).

[12] C. O. Avci, K. Garello, A. Ghosh, M. Gabureac, S. F. Alvarado, and P. Gambardella, Unidirectional spin Hall magnetoresistance in ferromagnet/normal metal bilayers, Nat. Phys. **11**, 570 (2015).

[13] T. Kodama, N. Kikuchi, S. Okamoto, S. Ohno, and S. Tomita, Spin-current driven permeability variation for time-varying magnetic metamaterials, Phys. Rev. Appl. **19**, 044080 (2023).

[14] T. Chiba, G. E. W. Bauer, and S. Takahashi, Current-induced spin-torque resonance of magnetic insulators, Phys. Rev. Appl. **2**, 034003 (2014).

[15] T. Chiba, M. Schreier, G. E. W. Bauer, and S. Takahashi, Current-induced spin torque resonance of magnetic insulators affected by field-like spin-orbit torques and out-of-plane magnetizations, J. Appl. Phys. **117**, 17C715 (2015).

[16] M. Schreier, T. Chiba, A. Niedermayr, J. Lotze, H. Huebl, S. Geprägs, S. Takahashi, G. E. W. Bauer, R. Gross, and S. T. B. Goennenwein, Current-induced spin torque resonance of a magnetic insulator, Phys. Rev. B **92**, 144411 (2015).

[17] S. Kasai, K. Kondou, H. Sukegawa, S. Mitani, K. Tsukagoshi, and Y. Otani, Modulation of effective damping constant using spin Hall effect, Appl. Phys. Lett. **104**, 092408 (2014).

[18] T. Nan, S. Emori, C. T. Boone, X. Wang, T. M. Oxholm, J. G. Jones, B. M. Howe, G. J. Brown, and N. X. Sun, Comparison of spin-orbit torques and spin pumping across NiFe/Pt and NiFe/Cu/Pt interfaces, Phys. Rev. B **91**, 214416 (2015).

[19] X. Fan, J. Wu, Y. Chen, M. J. Jerry, H. Zhang, and J. Q. Xiao, Observation of the nonlocal spin-orbital effective field, Nat. Commun. **4**, 1799 (2013).

[20] S. Karube, N. Tezuka, M. Kohda, and J. Nitta, Anomalous spin-orbit field via the Rashba-Edelstein effect at the W/Pt interface, Phys. Rev. Appl. **13**, 024009 (2020).

[21] G. A. Slack, Thermal conductivity of pure and impure silicon, silicon carbide, and diamond, J. Appl. Phys. **35**, 3460 (1964).

[22] W. Zhu, G. Zheng, S. Cao, and H. He, Thermal conductivity of amorphous $SiO_2$ thin film: A molecular dynamics study, Sci. Rep. **8**, 10537 (2018).

[23] S. Stackhouse, L. Stixrude, and B. B. Karki, Thermal conductivity of periclase (MgO) from first principles, Phys. Rev. Lett. **104**, 208501 (2010).

[24] See Supplemental Material at http://link.aps.org/supplemental/10.1103/PhysRevB.109.214419 for effects of substrate and Pt-Py strip length and evaluation of Oersted field, FLT effective field, and current density, which includes Refs. [18,21–23].

[25] S. Hirayama, S. Kasai, and S. Mitani, Interface perpendicular magnetic anisotropy in ultrathin Ta/NiFe/Pt layered structures, Jpn. J. Appl. Phys. **57**, 013001 (2018).

[26] K.-J. Kim, T. Li, S. Kim, T. Moriyama, T. Koyama, D. Chiba, K.-J. Lee, H.-W. Lee, and T. Ono, Possible contribution of high-energy magnons to unidirectional magnetoresistance in metallic bilayers, Appl. Phys. Express **12**, 063001 (2019).

[27] I. V. Borisenko, V. E. Demidov, S. Urazhdin, A. B. Rinkevich, and S. O. Demokritov, Relation between unidirectional spin Hall magnetoresistance and spin current-driven magnon generation, Appl. Phys. Lett. **113**, 062403 (2018).

[28] C. C. Chiang, S. Y. Huang, D. Qu, P. H. Wu, and C. L. Chien, Absence of evidence of electrical switching of the antiferromagnetic Néel vector, Phys. Rev. Lett. **123**, 227203 (2019).

[29] R. B. Belser and W. H. Hicklin, Temperature coefficients of resistance of metallic films in the temperature range 25 to 600 °C, J. Appl. Phys. **30**, 313 (1959).

[30] C. O. Avci, J. Mendil, G. S. D. Beach, and P. Gambardella, Origins of the unidirectional spin Hall magnetoresistance in metallic bilayers, Phys. Rev. Lett. **121**, 087207 (2018).

[31] T. Holstein and H. Primakoff, Field dependence of the intrinsic domain magnetization of a ferromagnet, Phys. Rev. **58**, 1098 (1940).

[32] K. Nakata, P. Simon, and D. Loss, Spin currents and magnon dynamics in insulating magnets, J. Phys. D **50**, 114004 (2017).

[33] C. W. Sandweg, Y. Kajiwara, A. V. Chumak, A. A. Serga, V. I. Vasyuchka, M. B. Jungfleisch, E. Saitoh, and B. Hillebrands, Spin pumping by parametrically excited exchange magnons, Phys. Rev. Lett. **106**, 216601 (2011).

[34] B. Divinskiy, S. Urazhdin, S. O. Demokritov, and V. E. Demidov, Controlled nonlinear magnetic damping in spin-Hall nano-devices, Nat. Commun. **10**, 5211 (2019).

[35] H. Fulara, M. Zahedinejad, R. Khymyn, M. Dvornik, S. Fukami, S. Kanai, H. Ohno, and J. Åkerman, Giant voltage-controlled modulation of spin Hall nano-oscillator damping, Nat. Commun. **11**, 4006 (2020).